Austrian Journal of Earth Sciences | Volume 103/1 | 101 - 110 | Vienna | 2010

High temperature corrosion of olivine phenocrysts in Pliocene basalts from Banat, Romania

Cornelius TSCHEGG[1)*)], Theodoros NTAFLOS[1)], Franz KIRALY[1)] & Szabolcs HARANGI[2)]

[1)] Department of Lithospheric Research, University of Vienna, Althanstr. 14, 1090 Vienna, Austria;

[2)] Department of Petrology and Geochemistry, Eötvös Loránd University, 1117 Budapest, Hungary;

[*)] Corresponding author, cornelius.tschegg@univie.ac.at

KEYWORDS

Cenozoic/Quaternary volcanism
high temperature corrosion
Carpatho-Pannonian Basin
olivine geochemistry
trachy-basalts

Abstract

Pliocene trachy-basalts from the eastern Pannonian Basin in Romania were studied to re-evaluate their petrogenesis and establish a new model for their eruption characteristics. Bulk major and trace element concentrations, as well as Sr and Nd radiogenic isotope ratios confirm their OIB type signature, totally unaffected and unrelated to precursor subduction activities in the Carpatho-Pannonian region. Late stage magmatic high temperature corrosion of olivine phenocrysts was analyzed in detail, using high-resolution electron-microprobe techniques. The data indicate that corrosion occurred shortly prior to eruption, due to interaction of the magma with groundwater. The triggered variation in oxygen fugacity results in an oxi-hydroxylised modification of the original structure of the olivine, which, after eruption and contemporaneous degassing of volatiles, was overgrown by fresh olivine rims.

Trachy-Basalte pliozänen Alters, die aus dem rumänischen Abschnitt des östlichsten Pannonischen Beckens stammen, wurden hinsichtlich ihrer Entstehung sowie ihrer speziellen Eruptionscharakteristik untersucht. Die Haupt- und Spurenelementzusammensetzungen dieser Gesteine sowie deren radiogenen Isotopenverhältnisse von Sr und Nd lassen eine typische OIB Signatur erkennen, ohne jegliche Beeinflussung durch vorangegangene Subduktionsaktivitäten in der Region. Besonderes Augenmerk dieser Studie gilt den Olivin-Phänokristallen der Laven, die mit Hilfe der Elektronenstrahlmikrosonde sehr detailliert analysiert wurden. In diesen Olivinphasen konnten magmatische Korrosionserscheinungen festgestellt werden, die vor Eruption dieser Basalte entstanden sind und eindeutig von gewöhnlichen Alterationserscheinungen unter Atmosphärenbedingungen zu unterscheiden sind. Die durch Kontakt des Magmas mit Grundwasser herbeigeführte Änderung der Sauerstoff-Fugazität noch im Erdinneren führte zu einer partiellen Hydro-Oxidation der Olivinstruktur, die nach der Eruption und der damit verbundenen Entgasung stoppte und somit einen randlichen Anwachssaum von frischem Olivin ermöglichte.

1. Introduction

Corrosion phenomena of olivine were observed by many authors in the past and linked to diverse alteration processes taking place at different atmospheric conditions and temperatures. Low temperature olivine weathering and iddingsitisation (LTI) is a well known process and was recently studied and reviewed by Velbel (2009 and references therein) and Clément et al. (2007 and references therein). It is understood as an alteration of olivine that postdates the eruption, therefore occurs under atmospheric conditions and results in a mixture of phyllosilicates and goethite. High temperature iddingsitisation (HTI) was lately reviewed by Clément et al. (2007) and interpreted as a magmatic alteration of olivine that affects mineral phases prior to eruption, in the magma chamber. Temporary increase of oxygen fugacity, participation of water and temperatures above 1075 °C leads to alteration of the olivine's chemical composition and mineral structure at the periphery of the grain, which is in the very late stage overgrown by fresh olivine after eruption and degassing. After Goff (1996), HTI alters olivine minerals to cryptocrystalline aggregates consisting of orthopyroxene, cristobalite, amorphous silica, maghemite and hematite. After eruption and associated pressure release, the oxygen fugacity rapidly decreases, resulting in simultaneous crystallisation of fresh olivine at the outermost rim of the phenocrysts as well as crystallisation of the groundmass constitutive minerals.

In this paper, we present alkaline lavas that indicate a systematic HTI-like corrosion phenomenon of olivine phenocrysts. Because we did not observe real iddingsite formation as described in Goff (1996), we decided to call this phenomenon high temperature corrosion (HTC) of olivine, to avoid confusion with HTI. Furthermore we present new geochemical data and petrogenetic ideas on Pliocene alkaline lavas from the Romanian part of the eastern Pannonian Basin.

2. Geological setting of the sampling locality

In the Carpatho-Pannonian Basin, Pliocene alkaline volcanic activity follows the Eocene to Pliocene subduction-related calc-alkaline volcanism in the Inner Carpathian arc (Downes et al., 1995). In Romania, Cenozoic/Quaternary alkaline activity can be found in two main areas – the Persani Mountains and Banat (Fig. 1). Banat lies on the easternmost extension of the Pannonian Basin, southwest of the Apuseni Mountains. The generation of the Pliocene Banat alkali basalts was reported being related to an asthenospheric reservoir that melted due to decompression along the South-Transylvanian fault system (Segehdi et al., 2004, and references therein).

Two main volcanoes exist in the Banat area, the alkaline ba-

salts in Lucaret-Sanovita and the lamproites in the region south of Gâtaia (Seghedi et al., 2008). In this study, four samples from the Sanovita quarry (N45°48‘45“, E21°42’35.7“) and two samples from the Lucaret quarry (N45°49‘14“, E21°41’19.5“) were taken and investigated in detail. Downes et al. (1995) analyzed one sample from Lucaret and another from Sanovita and dated these lavas to 2.5 Ma and 2.6 Ma (both K-Ar), respectively, so that these volcanic rocks overlap the Pliocene/Quaternary boundary interval. The Banat volcano mainly comprises lavas that lie on pyroclastic deposits and are themselves overlain by strombolian deposits (Downes et al., 1995).

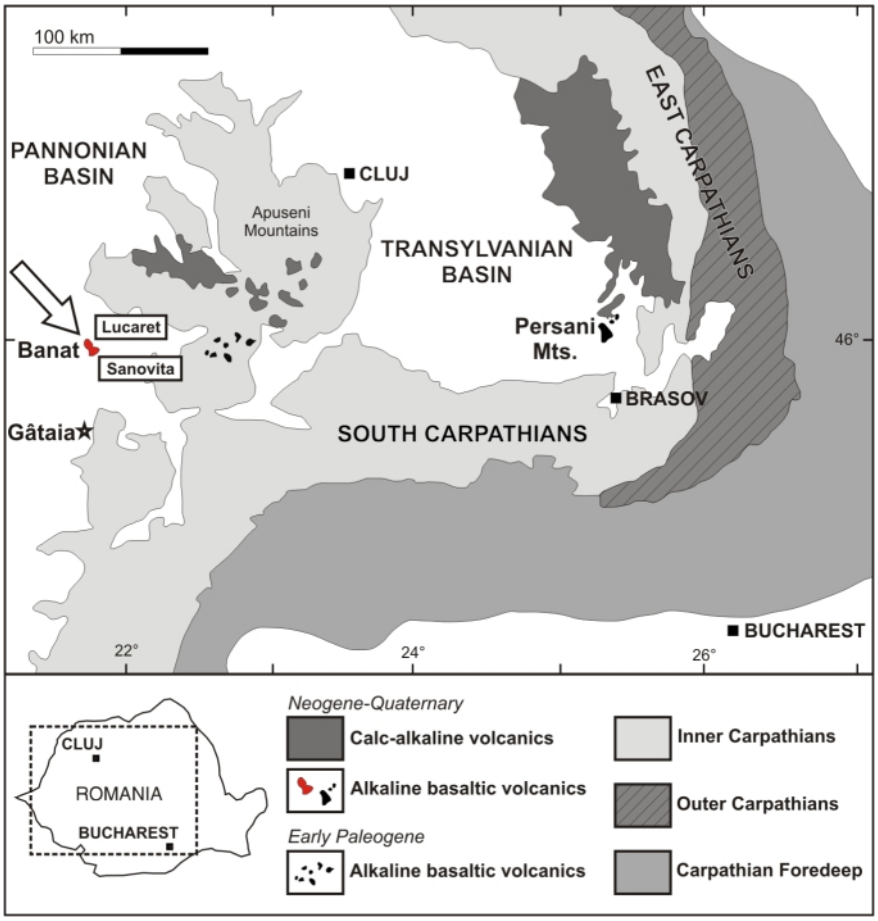

Figure 1: Simplified geological overview of Romania (after Downes et al., 1995 and Seghedi et al., 2008).

3. Analytical procedures

Mineral and HTC compositions were analyzed using a Cameca SX-100 electron microprobe (Department of Lithospheric Research, University of Vienna) equipped with an energy- and four wavelength-dispersive spectrometers on polished thin sections. ZAF standard corrections were applied to all acquired data.

Spot and line measurements were performed against natural standards with an acceleration voltage of 15 kV and a beam current of 20 nA. To obtain sufficient resolution of element variations within the grains, rim-to-rim measurements were made with a point distance of 5-7 µm by stage in step-mode in the rimzones. In the core sections, the point distance was increased to 10-30 µm step-size. Smaller grains were thoroughly analyzed with 5-78 µm step-size. The elements were measured in fixed sequential order with following peak/+-background times: Spectrometer 1: Si ka (TAP) 20s/5s, Mg ka (TAP) 20s/10s; Spectrometer 2: Mn ka (LLiF) 20s/5s, Fe ka (LLiF) 20s/5s, Ni ka (LLiF) 40s/25s; Spectrometer 3: Al ka (TAP) 70s/45s; Spectrometer 4: Ca ka(PET) 70s/45s; The resulting detection limits for trace elements are 80 for Al_2O_3, 135 ppm for CaO, 500 ppm for MnO and 400 ppm for NiO. For the major elements MgO, SiO_2 and FeO, a relative error below 5% can be assumed.

For the performed element mappings, working conditions were 25 kV accelerating voltage and 60 nA beam current. The beam was focused and fixed, while the stage moved the sample continuously with a dwell-time of 100 ms. The final resolution of the images are 512x384 pixel. The images for trace elements Al, P, Ca and Ni were acquired with the WDS spectrometers, because they have much lower detection limits than the built-in EDS detector. Mg, Si, Mn, Fe mappings were acquired on EDS simultaneously with the mentioned trace elements on the WDS spectrometers.

To determine bulk major element abundances, fused beads were prepared with a 1:5 sample to flux (di-Lithium tetra-Borate) mixture and analyzed with a sequential X-ray fluorescence spectrometer PW 2400 (Department of Lithospheric Research, University of Vienna). Bulk trace element analyses were carried out on pressed powder pills.

Single trace and rare earth elements were measured on a Perkin Elmer ELAN 6100 DRC ICP-MS (Department of Lithospheric Research, University of Vienna; Division of Analytical Chemistry, University of Natural Resources and Applied Life Sciences, Vienna). All specimens were digested in Teflon beakers following the method described in Tschegg et al. (2008). The dissolved samples were diluted in a 2 % HNO_3 solution with a Li-Rh-In-Bi internal standard mixture. For external calibration multiple dilutions of the geological standard sample BCR-2 were analyzed, produced following the digestion procedure of the sample specimens. Further geo-reference samples (BHVO-2 and DTS-1) were repeatedly analyzed for quality assessment.

Sr and Nd isotopic analytical work was performed on a ThermoFinnigan Triton TI Tims at the Department of Lithospheric Research (University of Vienna) adhering the sample prepara-

tion and analytical procedure described in Thöni et al. (2008).

4. Bulk major- and trace-element composition and radiogenic isotopes

Bulk major and trace element concentrations of the studied basalts are summarized in Table 1 and illustrated in Fig. 2a and 2b. According to the TAS (Total Alkali-Silica) diagram (Fig. 2a), the studied lavas, from Sanovita as well as from Lucaret, all plot in the trachy-basalt field. The silica-saturated rocks (SiO_2 49.1-49.6 wt.%) vary within a narrow compositional range. MgO varies from 7.9 to 8.6 wt.%, Al_2O_3 from 14.6 to 14.9 wt.% and CaO from 8.6 to 9.1 wt.%. TiO_2 (around 2.3 wt.%) and P_2O_5 (around 0.6 wt.%) concentrations are generally low in the slightly evolved trachy-basalts.

The Banat trachy-basalts indicate no linearity concerning compatible trace elements, they have Ni concentrations around 122-139 ppm and Cr around 168-184 ppm. The Sr concentration range is considerably marginal in these rocks (619-649 ppm), Rb ranges from 34 to 37 ppm and Ba from 454 ppm to 514 ppm. In the primitive mantle normalized spider diagram (Fig. 2b), a very consistent and homogeneous trend is indicated for the trachy-basalts showing no significant anomalies. Only Pb indicates a slight positive anomaly compared to the neighbouring elements Ce and Sr. A tendency of highly incompatible element enrichment and less incompatible element depletion is comprehensible (La_N/Sm_N 2.6, La_N/Yb_N 6.1-6.4) showing correlation with typical OIB (Ocean Island Basalt) lavas (Fitton, 1991). The analyzed samples are almost identical to the alkaline basalts investigated by Downes et al. (1995).

The alkaline basalts indicate a slightly enriched isotopic signature with $^{87}Sr/^{86}Sr$ ranging between 0.7035 and 0.7036 and $^{143}Nd/^{144}Nd$ ratios around 0.51280, also almost identical with the data presented in Downes et al. (1995). Present day epsilon Nd values plot close to the European Asthenospheric Reservoir (Cebria and Wilson, 1995).

5. Optical microscopy and EPMA observations

Since the neighbouring lavas at Sanovita and Lucaret belong to the same volcano, their mineral assemblages and mineral textures and compositions are hardly distinguishable, as previously noted for the bulk-rock compositions. Representative compositions of the main included mineral phases are therefore summarized in Table 2. Porphyritic intergranular textures

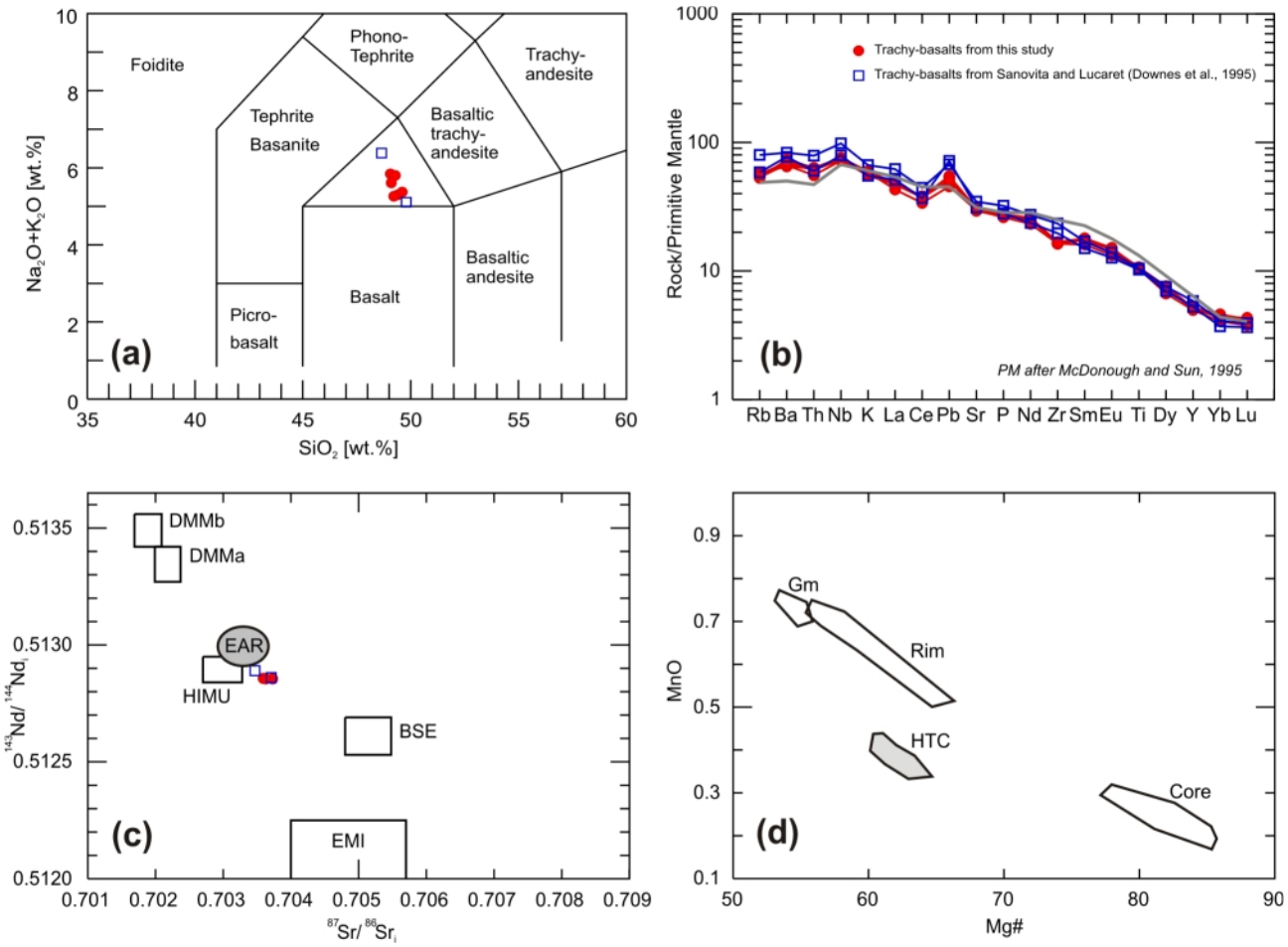

Figure 2: Bulk major and trace element composition and radiogenic isotope ratios of the Banat lavas. (a) TAS (Total Alkali-Silica) diagram after Le Bas et al. (1986), (b) Primitive mantle normalized spider diagram (OIB composition from Sun and McDonough, 1989 indicated in grey), (c) $^{87}Sr/^{86}Sr$ vs. $^{143}Nd/^{144}Nd$ (EAR – European Asthenospheric Reservoir after Cebria and Wilson, 1995). (d) Outlined fields comprise EPMA olivine analyses, Mg# vs. MnO of core and rim sections in the phenocrysts, groundmass olivines (Gm) and the high temperature corrosion (HTC) zones.

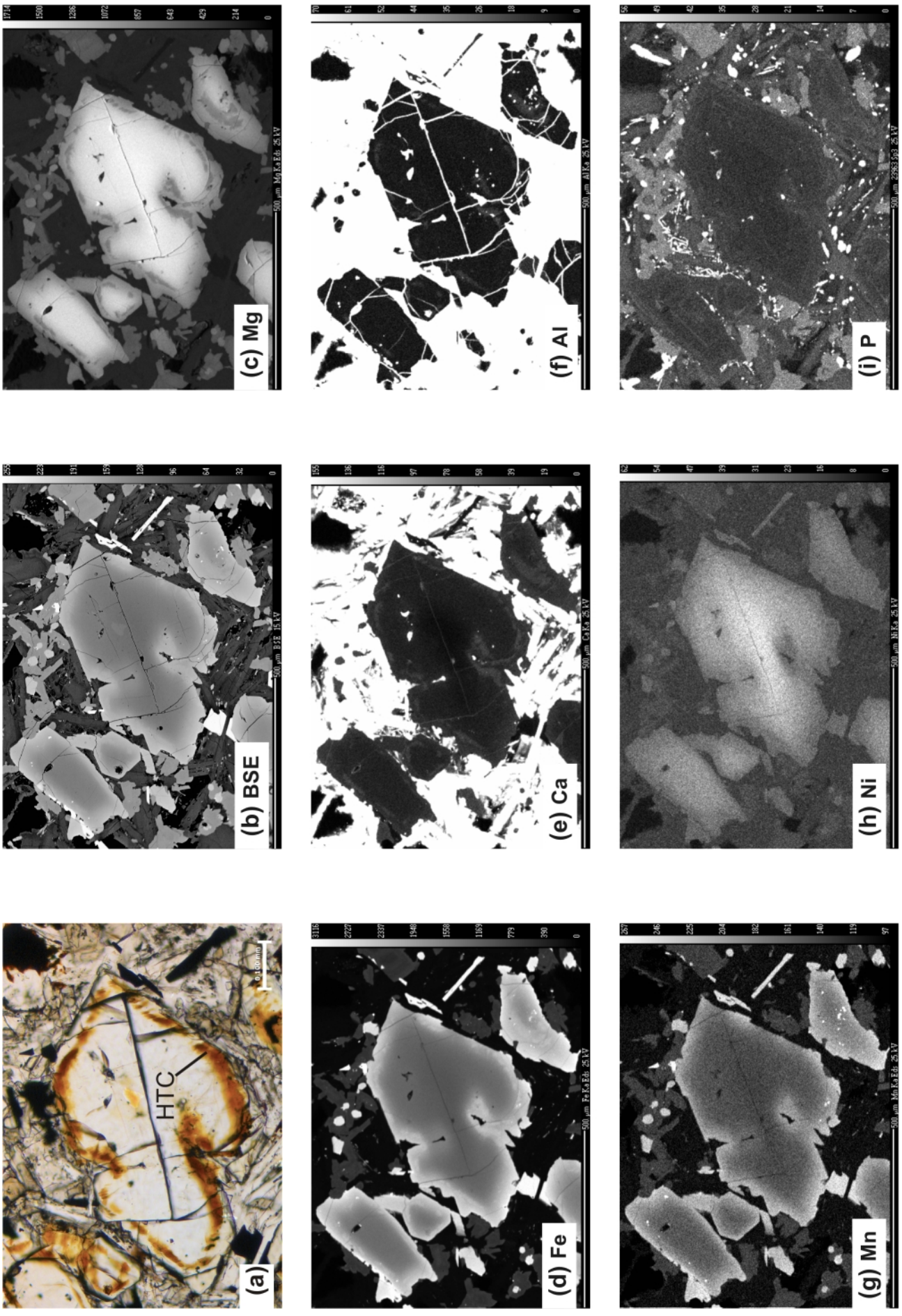
(a)
HTC
0.100 mm
(b) BSE
(c) Mg
(d) Fe
(e) Ca
(f) Al
(g) Mn
(h) Ni
(i) P

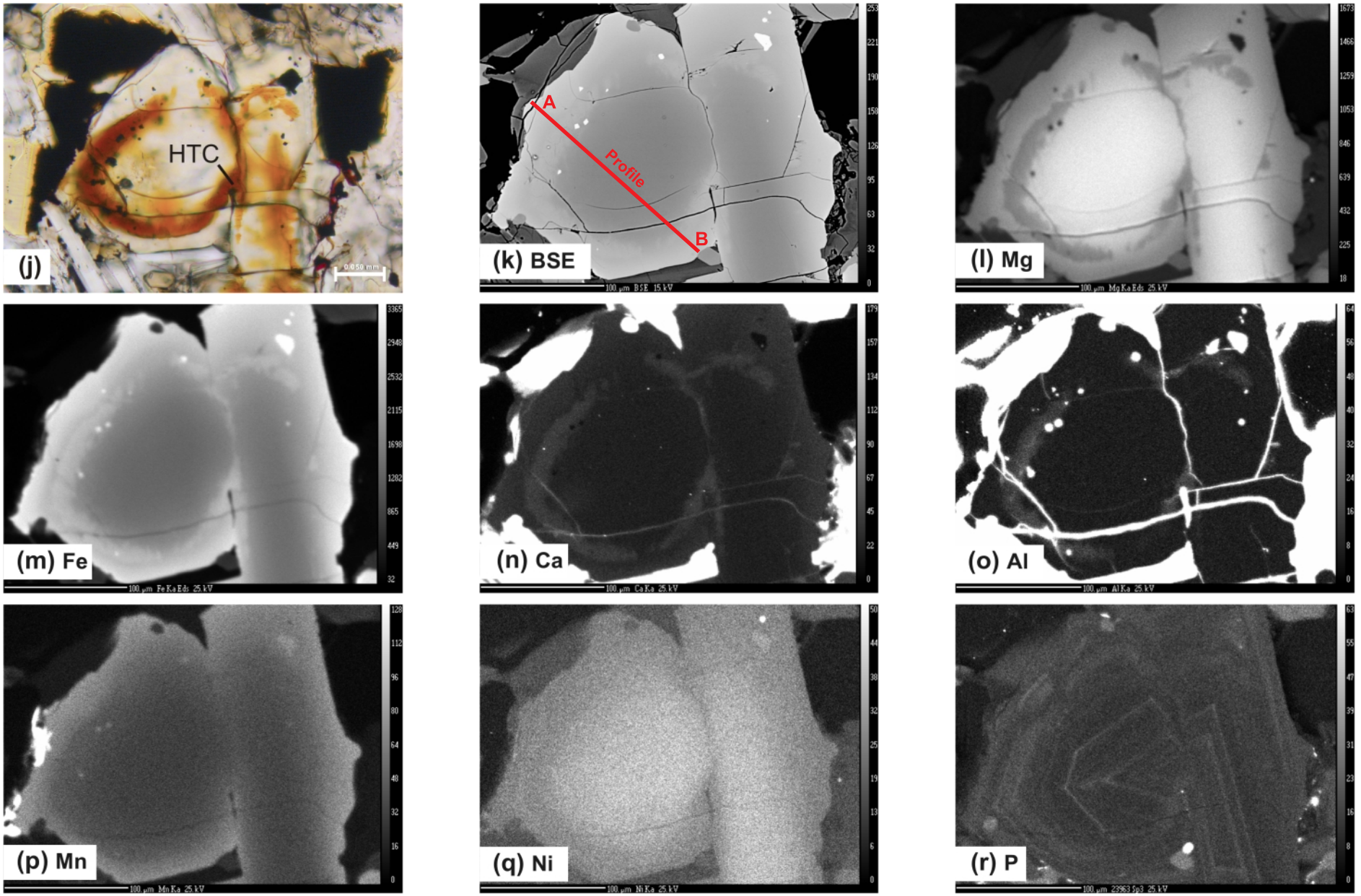

Figure 3: Photomicrographs, EPMA backscattered-electron images and EPMA element mappings of two representative olivine phenocrysts of the Banat lavas. (a, j) photomicrographs; (b, k) BSE images; (c, l) Mg mappings; (d, m) Fe mappings; (e, n) Ca mappings; (f, o) Al mappings; (g, p) Mn mappings; (h, q) Ni mappings; and (i, r) P mappings.

can be observed in the lavas, with slightly varying amounts of olivine as well as clinopyroxene phenocrysts embedded in a groundmass of mainly plagioclase laths intergrown by clinopyroxene. Almost throughout, the samples are vesicular. Idiomorphic to subidiomorphic olivine phenocrysts are in general large, their size varies from 100 to 800 μm and sometimes exceed the 1000 μm diameter. They have compositions with Fo_{81-85} in the core and Fo_{59-61} in the rim, CaO is around 0.2 wt.% in the core rising to 0.4-0.5 wt.% in the rim. Groundmass olivines have Fo around 53-55 and CaO concentrations of 0.5 wt.% without any compositional zoning. Clinopyroxene phenocrysts have Mg# [100x(Mg/Mg+Fe)] 77-78 and $En_{40-43}Wo_{40-45}Fs_{12}$. Their equivalents in the groundmass have Mg#s ranging from 74 to 79 and $En_{39-43}Wo_{45-46}Fs_{11-14}$. Other dominant groundmass minerals are plagioclases ranging in composition from $Ab_{24}An_{75}Or_1$ to $Ab_{92}An_2Or_6$, Ti-magnetite (TiO_2 around 25 wt.% and FeO around 67 wt.%), ilmenite (TiO_2 around 51 wt.% and FeO around 44 wt.%), spinel (Cr# around 50 as a groundmass constituents and Cr# [100x(Cr/Cr+Al)] 43 when included in olivine phenocrysts). Accessory apatite and glass can also be found.

The olivine phenocrysts throughout indicate a reddish-brown alteration affecting only the perimeter of the grains. The alteration zone itself is systematically rimmed by unaltered fayalitic olivine. Cracks and fractures that are visible in the grains are spared by this alteration process, such as all other mineral phases in the rock. Similar textural observations have been described by Goff, 1996, Caroff et al., 1999 and Clément et al, 2007 and interpreted as magmatic oxidation of olivine. To visualize the effect, two representative olivines grains were selected and analyzed with the polarizing microscope and the EPMA (Electron Probe micro-analyzer). The photomicrographs in Fig. 3a and 3j clearly indicate the fresh olivine core, the adjacent reddish-brown zone of corrosion (HTC) and the outermost fresh olivine rim. Thermal retraction cracks in the olivines are visibly unaltered and crosscut the corrosion zone, so that they must have been formed after the alteration process. In the BSE images of Fig. 3b and 3k, the zoning from a more forsteritic composition in the core (darker shading) to a more fayalitic composition in the rim (lighter shading) is visible; the enclosed zone of corrosion is recognizable as an area with somewhat lighter grey nuances and hardly visible but prevalent microcracks. The qualitative high-resolution element mappings illustrate the spatial distribution of concentrations in the corrosion zone and the fresh olivine as well. The HTC zone, compared to the fresh olivine, is characterized by low Mg (Fig. 3c, l) and enriched Fe (Fig. 3d, m) concentrations. In Figs. 3e and 3n as well as 3f and 3o, the elevated concentration of Ca and Al in the corrosion zone suggests similar to Fe behavior. Due to higher detection limits and the low concentrations of Mn (Fig. 3g, p) and Ni (Fig. 3h, q), their X-ray mappings do not provide unequivocal elemental distribution differences between HTC zone and fresh olivine. Nevertheless, concerning Mn a slight step of concentration increase is observable from the core to the rim in the corrosion zone, contrarily to Ni where an abrupt step in concentration decrease can be seen from the core to the rim. The studied olivines contain very low concentrations of phosphorous with unique oscillatory zoning (Fig. 3i, r). Further, an enrichment of P is visible in the corrosion zone compared to the fresh olivine, but not as clearly as for other elements. Si mappings were carried out but are not illustrated in Fig. 3 as they do not show any significant compositional variation.

A representative quantitative rim-to-rim line profile in an olivine grain (its position is indicated on the BSE image in Fig. 3k) is given in Fig. 4. Out of several analyzed olivines, this grain was

	SANOVITA				LUCARET	
	DV48	DV49	DV50	DV51	DV52	DV53
XRF measurements [wt.%]						
SiO_2	49.4	49.1	49.6	49,2	49.3	49.1
TiO_2	2.26	2.25	2.32	2.25	2.25	2.28
Al_2O_3	14.7	14.7	14.9	14.6	14.6	14.7
FeO^t	9.91	9.80	10.1	9.95	9.81	9.91
MnO	0.16	0.15	0.16	0.16	0.15	0.15
MgO	8.55	8.44	7.94	8.57	8.61	8.36
CaO	8.80	8.56	8.92	9.07	8.65	8.62
Na_2O	3.61	4.08	3.57	3.60	4.03	3.90
K_2O	1.69	1.76	1.80	1.66	1.77	1.71
P_2O_5	0.59	0.58	0.60	0.58	0.57	0.58
Total	99.6	99.3	99.9	99.7	99.7	99.3
LOI	0.15	-0.32	0.33	0.42	-0.40	-0.18
Mg#	60.6	60.6	58.4	60.6	61.0	60.1
XRF measurements [ppm]						
Nb	52.4	53.0	54.0	52.1	51.4	52.1
Zr	183	184	189	183	183	184
Y	23.0	23.0	23.6	23.1	22.6	23.1
Sr	649	619	639	638	627	636
Rb	34.6	36.8	33.6	34.0	36.0	35.8
Ga	22.2	21.7	21.4	21.8	22.2	23.0
Zn	85.3	94.3	96.7	89.2	85.9	88.2
Cu	40.5	43.2	43.3	44.4	46.1	45.0
Ni	122	136	136	125	138	139
Co	41.8	44.5	44.3	42.1	41.4	42.5
Cr	168	184	181	171	177	179
Sc	9.9	10.0	10.7	8.4	10.1	10.9
V	139	150	153	145	144	140
Ba	497	454	514	473	464	492
ICP-MS measurements [ppm]						
Cs	0.39	0.56	0.47	0.41	0.55	0.53
La	32.9	33.0	33.2	32.4	29.5	33.0
Ce	67.0	67.4	67.7	66.1	60.0	66.9
Pr	8.57	8.56	8.59	8.35	7.61	8.52
Nd	35.0	35.2	35.1	34.2	31.5	34.9
Eu	2.53	2.54	2.51	2.46	2.23	2.51
Sm	7.97	7.92	7.95	7.73	7.12	7.95
Gd	7.05	7.08	7.09	6.89	6.28	7.00
Tb	1.06	1.07	1.05	1.03	0.94	1.06
Dy	5.57	5.52	5.60	5.43	4.92	5.48
Ho	1.07	1.04	1.05	1.02	0.94	1.03
Er	2.69	2.66	2.69	2.59	2.38	2.62
Tm	0.37	0.36	0.37	0.35	0.31	0.36
Yb	2.20	2.25	2.27	2.16	2.00	2.17
Lu	0.31	0.31	0.31	0.31	0.28	0.32
Ta	3.12	3.19	3.15	3.04	2.85	3.13
Pb	3.88	3.82	3.83	3.59	3.23	3.59
Th	5.30	5.35	5.39	5.22	4.72	5.26
U	1.49	1.45	1.12	1.29	1.35	1.50
Radiogenic isotope ratios						
$^{87}Sr/^{86}Sr$			0.703730		0.703590	0.703628
$^{143}Nd/^{144}Nd$			0.512855		0.512857	0.512855

FeOt = total amount of iron;

Table 1: Whole-rock compositions and Sr-Nd radiogenic isotope ratios of Banat trachy-basalts

chosen because it is relatively small in size and therefore allows a detailed illustration of the elemental concentrations. Fig. 4a shows the distribution of the major elements SiO_2, MgO and FeO as well as the totals of the analyses. Olivine shows magmatic zonation with symmetric elemental distribution across the analyzed grain. The MgO contents decrease from core (Fo_{82}) to rim (Fo_{57}) with a sharp drop in the corrosion zone. With a concentration trough in the perimetric HTC zone, MgO shows the most intensive affection due to corrosion concerning major elements (minus 3-6 wt.%). The corrosion zone at the perimeter of the olivine, indicated by the grey shade, ranges from approx. 15 µm to 30 µm distance from both grain boundaries. Within this HTC ring, a loss of total analytical sum of 3-5 % is recognizable. SiO_2, which normally tends to decrease towards the grain boundary, indicates a flattening in the corrosion affected zone. As FeO behaves contrary to MgO in the olivine system, it signifies a slight but anomalous increase of concentration in the HTC zone, this trend normalizes against the rim.

Turning to the obtained trace element abundances and patterns, Al_2O_3, though weakly, and CaO show a considerable enrichment within the HTC ring. Al_2O_3 contents increase tenfold compared to the adjacent unaffected grain, CaO increases more than 1.5-fold compared to the surrounding core and rim sections. NiO that normally behaves like MgO, lowering its concentration from the core towards the boundaries, shows a stepped decrease in the corrosion zone when tracked from core to rim. MnO illustrates the contrary trend, a stagnating increase of concentration in the HTC zone, jumping abruptly up to approx. 0.2 wt.% higher amounts after the HTC.

Fig. 2d and Table 2 provide a compositional overview of observed olivine core, HTC, olivine rim and groundmass olivine chemistries. It is indicated first that the observed outermost rim compositions of the measured olivines are very similar and partly overlap with the olivine compositions analyzed in the groundmass. Second, it points out the systematic depletion of MnO concentration for the given Mg# or FeO respectively, which are normally strongly correlated in the olivine composition (Leemann and Scheidegger, 1977).

	OLIVINE				CLINOPYROXENE				PLAGIOCLASE			Ti-MAG	SPINEL	SPINEL	ILMENITE
	Ph		Gm	HTC	Ph		Gm			Gm		Gm	Gm	In olivine	Gm
	core	rim			core	rim									
SiO_2	38.9	35.7	35.1	36.2	48.7	47.9	50.3		SiO_2	52.3	52.2	24.6	15.4	4.85	51.3
Al_2O_3	0.03	0.04	0.04	0.14	1.86	2.33	1.67		Al_2O_3	29.0	29.5	1.23	6.24	15.5	0.06
Cr_2O_3	b.d.l.	0.02	b.d.l.	b.d.l.	4.69	4.70	2.60		FeO^t	0.69	0.64	0.05	13.0	24.9	0.02
FeO^t	17.4	33.2	37.5	30.3	0.03	0.37	0.07		CaO	12.2	0.26	67.3	55.8	38.3	44.1
MnO	0.26	0.62	0.69	0.35	7.14	7.05	7.04		Na_2O	4.41	16.0	0.64	0.51	0.27	0.69
MgO	42.5	28.8	25.5	27.7	0.13	0.16	0.14		K_2O	0.26	1.74	1.97	3.29	6.59	2.15
CaO	0.24	0.40	0.54	0.46	14.0	13.5	14.6		BaO	0.12	0.03	0.01	0.07	0.09	0.03
NiO	0.22	0.04	0.01	0.09	22.4	22.3	22.0		Total	99.1	100.6	95.9	94.6	94.8	98.5
Total	99.6	98.8	99.4	95.2	0.40	0.46	0.45					1.8	49.7	43.1	13.6
Mg#	81.4	60.8	54.8	61.9	99.3	98.8	98.9					5.0	9.5	23.5	8.0
					77.8	77.4	78.7								
	Formula based on 3 cations				Formula based on 4 cations				Formula based on 5 cations			Formula based on 3 cations			4 cations
Si	0.994	0.996	0.997	1.046	1.814	1.801	1.883		Si	2.400	2.155	Ti	0.696	0.428	0.131	1.963
Al	0.001	0.001	0.001	0.005	0.206	0.208	0.115		Al	1.566	1.435	Fe^{3+}	0.551	0.492	0.379	0.000
Fe^t	0.370	0.774	0.890	0.733	0.222	0.221	0.220		Fe^t	0.026	0.022	Cr	0.001	0.380	0.704	0.001
Mg	1.618	1.200	1.078	1.192	0.052	0.066	0.047		Na	0.392	1.284	Al	0.055	0.272	0.655	0.004
Mn	0.006	0.015	0.017	0.009	0.001	0.011	0.002		Ca	0.598	0.011	Fe^{2+}	1.565	1.231	0.770	1.876
Ca	0.007	0.012	0.016	0.014	0.779	0.759	0.816		K	0.015	0.092	Mg	0.111	0.181	0.352	0.163
Ni	0.004	0.001	0.000	0.002	0.004	0.005	0.005		Ba	0.002	0.001	Mn	0.020	0.016	0.008	0.030
					0.029	0.033	0.033								
					0.893	0.896	0.881								

FeO', Fe' = total amount of iron; Mg# = 100 x molar (MgO+FeO')/MgO; Cr# = 100 x molar $(Cr_2O_3+Al_2O_3)/Cr_2O_3$; b.d.l. beyond detection limit; Ph = Phenocrysts; Gm = Groundmass; HTC = High Temperature Corrosion;

Table 2: Representative EPMA mineral and HTC compositions of the Banat trachy-basalts

6. Discussion

The Pliocene trachy-basalts from Banat reflect a very narrow range of chemical composition. Although they indicate involvement of differentiation processes, according to their major- and trace-element chemistry and radiogenic isotope composition, these rocks clearly represent OIB-type lavas. The high HFSE contents together with the lack of negative Nb and Ti anomalies and the depleted radiogenic isotopes, in general suggest absence of any subduction-related material during magma generation, and imply a relatively small degree of melting of an asthenospheric source. Since the trachy-basalts are, even if slightly, differentiated rocks, their melt generation and evolution is hard and quite arguable to ascertain. The lavas from this study show strong similarities with other alkaline basalts from Banat and the Quaternary alkaline basalts from the western Pannonian Basin investigated by Downes et al. (1995) and Embey-Isztin et al. (1993), respectively.

The vesicular lavas contain olivine phenocrysts indicating corrosion processes at their grain perimeter, rimmed by ferrous newly formed olivine, a phenomenon which is not observable for the clinopyroxene phenocrysts. Due to the fresh

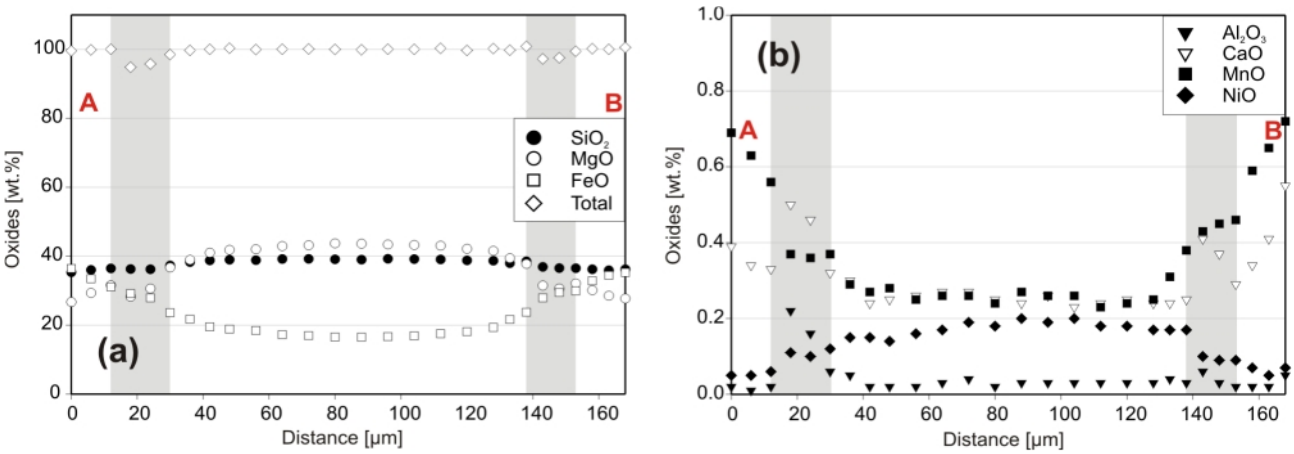

Figure 4: EPMA line measurement through an representative olivine phenocryst with high temperature corrosion. Position of the profile shown in Fig. 3k. Major oxides SiO_2, MgO, FeO and the analytical total are illustrated in Fig. 4a, Al_2O_3, CaO, MnO and NiO in Fig 4b. Areas of light grey shading indicate the sections of HTC.

fayalitic olivine overgrowth at the outermost rim and the fact that thermal retraction cracks do not indicate corrosion, low temperature iddingsitisation can clearly be excluded. The zones of corrosion are limited in size (around 15-20 µm) and do not show exsolution of any new mineral phases. According to these observations, also no evidence was found that a complete high temperature iddingsitisation alteration took place, as it was described by Goff (1996).

Both line measurements and element mappings, show that the normal igneous growth/ zoning of the investigated olivine phenocrysts is interrupted by a short period of magmatic HTC, taking place during magma evolution. This period of alteration is comprehensible on the basis of elemental changes within the HTC zone and the conspicuous decrease of the analytical sum. Our quantitative observations show that the analytical deficit in the HTC zone is a result of three combined factors: (a) Loss of element excitation potential during measurements due to higher porosity, (b) presence of Fe^{3+} in the altered structure of olivine, which when calculated to FeO^{total} based on Fe^{2+} lowers the total analytical sum and finally (c) incorporation of H_2O into the mineral structure. This so-called oxi-hydroxylation of olivine or laihunitisation combined with water incorporation was also suggested by former authors as a major process of olivine corrosion under magmatic conditions (see Clément et al., 2007). Being aware that the HTC zone has a distorted olivine stoichiometry, a formula calculation based on olivine is given in Table 2. Due to expected incomplete chargebalance though, the calculated structural formula of the HTC analysis gives excess Si. Nevertheless, the cationic deficit due to oxidation of Fe in the octahedral sites (Mg + Fe = 1.9 and Si / (Si + Mg + Fe) = 0.35) is consistent with the synthetic structural formula proposed for this corrosion product by Clément et al. (2007), reflecting a moderate oxi-hydroxylation process.

The systematic depletion of MnO at given amounts of total Fe (Fig. 2d) provides the evidence that part of the total iron is converted to the oxidized Fe^{3+} state in the HTC zone (FeO^{total} decreases around 3 wt.% from the olivine rims to the HTC zones).

Looking at the element mappings in Fig. 3, the corrosion process is most visible for the major divalent cations Mg and Fe but also for Ca and Al, despite their low concentrations in olivine. The analytical resolution for Mn and Ni is reduced due to higher detection limits what results in elevated background noise.

Other striking evidences against advanced iddingsitisation sensu-stricto and associated transformation of olivine into new mineral phases, are the remaining cation proportions and the continuing oscillatory zoning of phosphorous (Fig. 3q and 3r) in the HTC affected areas of the investigated olivines. Beside the discussed systematic change in iron concentration, the oxide proportions are hardly affected by the corrosion process. The normal igneous zoning in the olivines is pointed out by line measurements as well as element mappings and is mainly represented by MgO and FeO. As mentioned, the zoning pattern is interrupted by the HTC. Despite the fact that olivine phenocrysts grow from a more forsteritic core composition to a more fayalitic rim composition, the internal phosphorous zoning is not correlated with these mentioned major constituents. Phosphorous in olivine is not a common feature. It reflects excess of phosphorus during rapid growth of the olivine phases. The oscillatory zoning patterns record crystal-growth-rate variations (Milman-Barris et al., 2008) and point to an igneous crystallisation that was not affected during the corrosion process. Mobilisation of P would requires persistent high temperatures due to the slow diffusion rates of phosphorous, destruction of the zoning could only be a result of recrystallisation or complete breakdown of the olivine phase (McCanta et al., 2009).

7. Conclusion

The Pliocene trachy-basalts from Sanovita and Lucaret represent OIB-type rocks with very limited compositional variations. They correlate well with other alkaline basalts from the Carpathian-Pannonian region of the same age, indicating no subduction-related influence.

Field observations of the studied lavas and the fact that

these are intercalated with, and possibly follow pyroclastic layers rich in volatiles, suggests that prior to eruption, hot magma reacted with infiltrating groundwater, but of an amount insufficient to trigger an immediate explosive phreatomagmatic eruption. The highly vesicular textures of the studied lavas confirm the pronounced presence of volatiles. Increased water contents and the resulting high oxygen fugacity during magma evolution, promoted high temperature corrosion (HTC) of already existing olivine phenocrysts. At this stage, prior to eruption, rim-near zones of olivine phenocrysts oxidized, became corroded and altered systematically in composition. After the critical increase of volatile pressure, the eruption of magma was triggered and gas release at surface conditions coupled with a drop in oxygen fugacity yielded the final growth of fresh olivine at the outermost rim of olivine phenocrysts, enclosing the studied HTC zones.

Acknowledgements

The authors want to thank the colleagues from the Department of Lithospheric Research (University of Vienna) Monika Horschinegg and Martin Thöni for the radiogenic isotope analyses and Peter Nagl for XRF measurements. The two referees, Alexander Proyer and Nino Seghedi, as well as the Editor Michael Wagreich, are gratefully acknowledged for substantially improving the manuscript.

References

Caroff, M., Guillou, H., Lamiaux, M., Maury, R.C., Guille, G. and Cotton J., 1999. Assimilation of ocean crust by hawaiitic and mugearitic magmas: an example from Eiao (Marquesas). Lithos 46, 235-258.

Cebria, J.M. and Wilson, M., 1995. Cenozoic mafic magmatism in western/central Europe: a common European asthenospheric reservoir? Terra Abstract, EUG 7, p. 162.

Clément, J.-Ph., Caroff, M., Dudoignon, P., Launeau, P, Bohn, M., Cotton, J., Blais, S. and Guille, G., 2007. A possible link between gabbros bearing High Temperature Iddingsite alteration and huge pegmatoid intrusions: The Society Islands, French Polynesia. Lithos 96, 524-542.

Downes, H., Seghedi, I., Szakaćs, A., Dobosi, G., James, D.E., Vaselli, O., Rigby, I.J., Ingram, G.A., Rex, D. and Pećskay, Z., 1995. Petrology and geochemistry of the late Tertiary/Quaternaryn mafic alkaline volcanism in Romania. Lithos 35, 65-81.

Embey-Isztin, A., Downes, H., James, D.E., Upton, B.G.J., Dobosi, G., Ingram, G.A., Harmon, R.S. and Scharbert, H., 1993. The petrogenesis of Pliocene alkaline volcanic rocks from the Pannonian Basin, eastern central Europe. Journal of Petrology 34, 317-343.

Fitton, J.G., James, D. and Leeman, W.P., 1991. Basic Magmatism Associated With Late Cenozoic Extension in the Western United States: Compositional Variations in Space and Time. Journal of Geophysical Research 96, B8, 13963-13711.

Goff, F.E., 1996. Vesicle cylinders in vapor-differentiated basalt flows. Journal of Volcanology and Geothermal Research 71, 167-185.

Le Bas, M. J., Le Maitre, R.W., Steckeisen, A. and Zanettin, B., 1986. A chemical classification of volcanic rocks based on the total alkali-silica diagram. Journal of Petrology 27, 745-750.

Leeman, W.P. and Scheidegger, K.F., 1977. Olivine/liquid distribution coefficients and a test for crystal–liquid equilibrium. Earth and Planetary Science Letters 35, 247-257.

McCanta, M.C., Beckett, J.R. and Stolper, E.M., 2009. Phosphorous zonation in H Chondrite olivines: The effects of increasing petrologic grade. 40th Lunar and Planetary Science Conference.

McDonough, W.F. and Sun, S.-s., 1995. The composition of the Earth. Chemical Geology 120, 223-253.

Milman-Barris, M., Beckett, J., Baker, M., Hofmann, A., Morgan, Z., Crowley, M., Vielzeuf, D. and Stolper, E., 2008. Zoning of phosphorus in igneous olivine. Contributions to Mineralogy and Petrology 155, 739-765.

Seghedi, I., Downes, H., Vaselli, O., Szakács, A., Balogh, K., Pécskay, Z., 2004. Post-collisional Tertiary-Quaternary mafic alkalic magmatism in the Carpathian-Pannonian region: a review. Tectonophysics 393, 43-62.

Seghedi, I., Ntaflos, Th., Pécskay, Z., 2008. The Gâtaia Pleistocene lamproite: a new occurrence at the southeastern edge of the Pannonian Basin, Romania. In: Coltorti, M., Grégoire, M. (Eds.), Metasomatism in Oceanic and Continental Lithospheric Mantle. Geological Society of London, Special Publication 293.

Sun, S. and McDonough, W.F., 1989. Chemical and isotopical systematic of oceanic basalts: implications for mantle composition and processes. In: Saunders, A.D., Norry, M.J. (Eds.), Magmatism in the Ocean Basins. Geological Society Special Publication, Vol. 42, 313-345.

Thöni, M., Miller, C., Blichert-Toft, J., Whitehouse, M.J., Konzett, J. and Zanetto, A., 2008. Timing of high-pressure metamorphism and exhumation of the eclogite type-locality (Kupplerbrunn-Prickler Halt, Saualpe, south-eastern Austria): constraints from correlations of the Sm-Nd, Lu-Hf, U-Pb and Rb-Sr isotopic systems. Journal of Metamorphic Geology 26, 561-581.

Tschegg, C., Hein, I. and Ntaflos, Th., 2008. State of the art multi-analytical geoscientific approach to identify Cypriot Bichrome Wheelmade Ware reproduction in the Eastern Nile delta (Egypt). Journal of Archaeological Science 35, 5, 1134-1147.

Velbel, M.A., 2009. Dissolution of olivine during natural weathering. Geochimica et Cosmchimica Acta 73, 6098-6113.

Received: 2. December 2009
Accepted: 17. February 2010

Cornelius TSCHEGG[1)*], Theodoros NTAFLOS[1)], Franz KIRALY[1)] & Szabolcs HARANGI[2)]

[1)] Department of Lithospheric Research, University of Vienna, Althanstr. 14, 1090 Vienna, Austria;

[2)] Department of Petrology and Geochemistry, Eötvös Loránd University, 1117 Budapest, Hungary;

[*)] Corresponding author, cornelius.tschegg@univie.ac.at